nature research

https://doi.org/10.1038/s41561-020-00660-6

Supplementary information

The role of environmental factors in the long-term evolution of the marine biological pump

In the format provided by the authors and unedited

Supplementary Materials

The role of environmental factors in the long-term evolution of the marine biological pump

1. A stochastic model for sinking rates of marine aggregates

To examine the effect of marine ecosystem evolution on the transfer efficiency of organic matter, we built a particle-based stochastic model of the biological pump. Our model calculates the age of organic particles in each aggregate based on their sinking rates and considers the impact of primary producer cell size, aggregation, temperature, dust flux, biomineralization, ballasting by mineral phases, oxygen, and the fractal geometry (porosity) of aggregates. The model provides a mechanistic framework for exploring the effects of redox change and ecosystem evolution on the efficiency of the ocean biological pump. Although this is a new model framework, this work builds on an extensive and solid foundation of modelling marine carbon fluxes[1–3].

The constitutive elements of our model are aggregates. These are represented as clusters of primary particles, a combination of phytoplankton cells (e.g., coccolithophorids, diatoms, picoplankton), and terrigenous dust particles (Main Text Fig. 1, Table S1). The model calculates the sinking rates of a large number of aggregates (10^6) at each depth. Dividing the ocean into 1000 depth intervals results in 10^9 aggregates in total, meant to roughly represent three-dimensional heterogeneity in the formation and destruction of individual aggregates across the ocean. The distribution of primary particles (dust particle, picoplankton, coccolithophorids, diatoms, etc.) in each aggregate is chosen according to the probabilities given in Table S1. The overall number of particles is corrected for the rate of aggregation at each depth.

By fully parameterizing the aggregation process in the model, we explored the effect of aggregation on the transfer efficiency of carbon. In the aggregation parameterization scheme, the number of particles at each depth is determined by a calculated aggregation rate. The probability of aggregation between two aggregates *i* and *j* ($P_{i,j}$) is defined as:

$$P_{i,j} = \gamma(z).\frac{\beta(i,j)}{\beta_{ref}}.\frac{F_{NPP}(z)}{F_{NPP_{ref}}}.\frac{F_{dust}(z)}{F_{dust_{ref}}} \quad (1)$$

where, β is the rate of collision between aggregates, γ is the aggregation efficiency parameter that varies with depth, *i*, and *j*, F_{NPP} and F_{dust} are the fluxes of net primary production and dust, and β_{ref}, $F_{NPPref,}$ $F_{dustref}$ are the reference values for collision rate, flux of net primary production, and dust flux, respectively. The last two parameters in the expression for probability of aggregation ($F_{NPP/}$ $F_{NPPref,}$ $F_{dust/}$ $F_{dustref}$) represent the higher probability of collision between aggregates at higher overall fluxes of primary particles from photosynthetic production and dust. The aggregation efficiency parameter, γ, is defined to decrease with depth, similar to the rate of organic matter degradation (following ref. 4). This assumption is based on observations in modern marine systems, where the primary substrate that holds marine snow together in the water column is transparent exopolymer particles (TEP) - a mucus-like polysaccharide material exuded by phytoplankton and bacteria. It has been suggested that production of these compounds

was highest under conditions of nutrient limitation during the senescent phase of phytoplankton blooms[1].

The overall rate of collision between two particles, β, is controlled by three mechanisms: very small particles mostly encounter each other by Brownian motion, whereas large particles meet each other due to fluid shear and differential settling (i.e., the larger particles settle faster sweeping up the smaller ones). In our model, similar to previous models[1], the coagulation kernel β is calculated as a sum of three mechanisms: collision frequency due to Brownian motion:

$$\beta_{Br} = \frac{8kT}{6\mu}\frac{(r_i+r_j)^2}{r_i r_j}, \quad (2)$$

fluid shear:

$$\beta_{sh} = 9.8\frac{q^2}{1+2q^2}\sqrt{\left(\frac{\varepsilon}{\nu}\right)}\left(r_i + r_j\right)^3, \quad (3)$$

where q = MIN (r_i , r_j) / MAX (r_i , r_j), and differential settling:

$$\beta_{ds} = \frac{1}{2}\pi\, MIN\left(r_{i\,,}\, r_j\right)^2\left|u_i - u_j\right| \quad (4)$$

[5,6]. Here k is the Stefan– Boltzman constant, μ is dynamic viscosity, ν is kinematic viscosity and ε is the turbulent dissipation rate set to 1×10^{-4} (ref. 1), while r_i and r_j are the radii of the two aggregates being evaluated for collision and u_i and u_j are the settling velocities of the two aggregates.

The averaged probability of aggregation at each depth is then used to determine the proportion of particles that are incorporated into aggregates in the following depth. For instance, at the very top of our domain where there is no aggregation, primary interacting particles (e.g. picoplankton, dust, etc.) are evaluated for aggregation, and average probability of aggregation at that depth is evaluated and used to determine what percentage of particles in the following depth will be contained within an aggregate.

2. Physical characteristics of aggregates

The volume of material in an aggregate is calculated as:

$$V_a = \alpha_1.\ V_C + \alpha_2.\ V_A + \alpha_3.\ V_{Di} + \alpha_1.\ V_{Pi} + \alpha_1.\ V_D + \alpha_1.\ V_{Ca} \quad (5)$$

where α is the number of primary particles in each aggregate, corrected for aggregate efficiency/probability of aggregation, and V is the volume of each primary particle, calculated using density and the total amount of material in each primary particle (Table S1).

An aggregate that forms by aggregation of smaller particles forms a fractal structure with a dimension, D_N, that describes its porosity: $p \sim r_a^{\,DN}$, where p is the number of primary particles in the aggregate and r_a is the radius of the aggregate[7]. The closer D_N is to 3, the more the

structure fills up three-dimensional space, and the lower its porosity. The fractal dimension of marine snow has been inferred from measurements of aggregate properties such as settling velocity, porosity and size, to be in the range of 1.3 to 2.3[7,8]. The aggregate radius, r_a, is then calculated using the fractal dimension and the radius of the primary particle, r_p:

$$r_a = r_p \cdot p^{1/DN}. \quad (6)$$

The radius of the primary particle, r_p, is calculated from its volume under the assumption that it is a sphere[1]:

$$r_p = \sqrt[3]{\frac{3V_p}{4\pi}}, \quad (7)$$

where V_p, the average volume of the primary particles in the aggregate, is calculated by dividing the total volume of material in the aggregate, V_a, by the number of primary particles in each aggregate:

$$V_p = \frac{V_a}{p}. \quad (8)$$

The aggregate porosity, φ, is related to the radius of individual particles that makes up the aggregate to the total radius of the aggregate:

$$\varphi = 1 - p\left(\frac{r_p}{r_a}\right)^3. \quad (9)$$

The density of the aggregate, ρ_a, is calculated using the density of the material in each aggregate, ρ_s, the density of seawater, ρ_{sw} and the porosity, φ:

$$\rho_a = (1-\varphi)\rho_s + \rho_{sw}, \quad (10)$$

where the density of the material in each aggregate, ρ_s is calculated as:

$$\rho_s = 1/p.(\alpha_1.\ \rho_C + \alpha_2.\ \rho_A + \alpha_3.\ \rho_{Di} + \alpha_1.\ \rho_{Pi} + \alpha_1.\ \rho_D + \alpha_1.\ \rho_{Ca}). \quad (11)$$

3. Sinking rate

Sinking rates of particles range from a few up to hundreds of meters per day[9] and have been found to increase with depth[10]. In our model, the sinking rate of an aggregate is calculated using Stokes' law[11]:

$$u = \sqrt{\frac{8r_a(\rho_a - \rho_{sw}).g}{3\rho_{sw}f(Re)}} \quad (12)$$

where g is the gravity of Earth. For low Reynolds numbers where viscous forces are dominant,

$$f(Re) = \frac{24}{Re} \quad (13)$$

and

$$Re = \frac{2r_a u}{\nu},$$

(14)

where ν is kinematic viscosity. For large Reynolds numbers where turbulence starts to play a role, the drag coefficient is calculated using Whites' approximation[12]:

$$f(Re) = \frac{24}{Re} + \frac{6}{(1+\sqrt{Re})} + 0.4\,,$$

(15)

which is valid for Re < 2 × 10^4. Substituting *f(Re)* with White's approximation results in a nonlinear equation that can be solved for *u*. Model aggregates are assumed to only sink vertically (i.e., there is no lateral current transport of aggregates). Aggregates reach high *Re* conditions when settling at a few hundred meters per day, depending on their size.

Within the range of salinity found in the modern seawater, the viscosity of seawater is mainly a function of temperature[13]. We use an expression that fits empirical data of seawater viscosity at 35 ppt to calculate the viscosity, ν, at temperature T [K][13]:

$$\nu = 5 \times 10^{-6}\, e^{\frac{2250}{T}} \qquad (16)$$

Seawater temperature is assumed to be constant within the upper mixed layer and changes linearly within the thermocline, followed by a linear change below the thermocline. This temperature structure mimics typical temperature-depth profiles in modern marine systems. Finally, the average sinking rate of aggregates at each depth is calculated by dividing the sum of sinking rate of aggregates to the total number of aggregates at each depth.

4. Zooplankton

Zooplankton in the model are grouped into small and large zooplankton based on their prosome length and their corresponding behavior (Fig. S1). Small zooplankton in the model interact with oceanic aggregates and can either fragment aggregates and result in smaller-sized aggregates or ingest them and produce a range of fecal pellet, consistent with the considered range of prosome length for them. Observation in the modern ocean shows an important role of particle aggregation in POC flux attenuation in the ocean mesopelagic zone[14]. Specifically, evidence of slow sinking oceanic aggregates in the modern deep ocean suggest an important role of disaggregation/fragmentation of the oceanic aggregates in marine biological pump. It has been suggested that fragmentation is mainly caused by turbulent flow in the ocean. However, experimental studies on oceanic aggregates revealed that larger stresses in excess of those due to turbulent shear in the ocean are needed to break the aggregates, suggesting that fragmentation caused by biological shear is the main control on aggregated fragmentation in the ocean[11]. This is also consistent with the observed decrease in the average size of oceanic aggregates when the zooplankton *Euphausia Pacifica* were abundant[15]. While the degree to which zooplankton influence the physical characteristics of the oceanic aggregates is not fully understood, experimental and modelling studies do confirm the fact that interaction between zooplankton and marine particles occurs and can lead to aggregate destruction. However, aggregate destruction is

restricted to clades of common zooplankton like copepods. Other reasonable common types of zooplankton, like salps, are predicted to induce minimal fragmentation [16].

Large zooplankton are further classed into non-migrating and migrating zooplankton. The migrating zooplankton are representative of zooplankton community that are able to vertically migrate into ocean twilight zone during the day and night, a process that is commonly known as Diel Vertical Migration (DVM), with consequent impact on POC flux and carbon transfer to depths. Generally, DVM is a movement of zooplankton to twilight zone during the day and swimming back to shallow waters during the night. There are number of environmental factors suggested to impact the DVM including water clarity, oxygen availability, seawater surface temperature, turbulence, and predator-prey interactions[17,18]. Modern observations indicate that DVM accounts for between 10 to 50% of the total vertical flux of carbon from shallow waters, suggesting an important role of DVM in transferring fixed carbon into ocean mesopelagic zone[19].

In the model, we first evaluate the possibility of encountering of oceanic aggregates with zooplankton and then depending on the zooplankton class, the aggregates can be fragmented (disaggregated) or ingested and produce range of faecal pellets. The calculated POC flux would then be corrected to account for the effect of DVM.

4.1. Encounter rate

While the encounter rate between the aggregates and zooplankton is not well constrained, we use the expression for the encounter rate of predator-prey interactions in zooplankton[20]. In the modern ocean the encounter rate for the predator and prey is suggested to be governed by two main processes: behavioural locomotion, E_B, and physical transport (e.g., turbulence), E_T. The former process reflects the effect of predator ability to autonomically move (swimming), whereas the latter process is a hydrodynamic process which can be further divided into the floating and turbulent mixing processes, both of which impact aggregation processes and the relative speed of the predator with respect to its prey. Thus, the overall encounter rate can be expressed as:

$$E = E_B + E_T \quad (17)$$

Under the assumption that the speed of the predator, v, exceeds that of the prey, u, E_B is parameterized as[21]:

$$E_B = \pi Z_p d^2 \frac{u^2+3v^2}{3v} \quad (18)$$

where d is the zooplankton's contact radius (i.e. the maximum distance at which the zooplankton can perceive aggregate), and Z_P is the aggregate concentration. Encounter rate as result of turbulent can also be expressed as[20]:

$$E_T = \pi Z_p d^2 w \quad (19)$$

where w is the linear orbital velocity of turbulent eddies (the turbulent velocity).

E_B correspond to the behavioural impact on the encounter rate and E_T relates the effect of turbulent to the encounter rate. To account for the contribution of microscale turbulence on the relative motion of predator and prey, the original encounter rate equation was revised, and the overall encounter rate recast as[20]:

$$E = \pi Z_p d^2 \frac{u^2 + 3v^2 + 4w^2}{3(v^2 + w^2)^{0.5}} \quad (20)$$

In our model, the encounter rate is defined as the ratio of the encounter rate calculated for each aggregate velocity, u_i, divided to the encounter rate calculated using the typical range of values (zooplankton speed, *v*, turbulent, *w*, and the aggregate velocity, *u*) suggested for the modern ocean. Assuming a relatively constant contact radius, *d*, for the modern and ancient oceans, the encounter rate can then be expressed as:

$$E_{total} = \frac{Z_{p_1} \frac{{u_i}^2 + 3v^2 + 4w^2}{3(v^2 + w^2)^{0.5}}}{Z_p \frac{u^2 + 3v^2 + 4w^2}{3(v^2 + w^2)^{0.5}}} \quad (21)$$

where Z_{p1} is the aggregate concentration in the ancient ocean. We assume that aggregate concentration, Z_p, is controlled by the strength of net primary production, and high net primary production results in higher aggregate concentrations. Equating the ratio of Z_p to the ratio of net primary production in the modern and ancient oceans ($Z_p/Z_{p1} = F_{NPP/} F_{NPPref}$), and assuming constant values for *v* and *w* throughout geologic time, the encounter rate can be rewritten as:

$$E_{total} = \frac{{u_i}^2 + 3v^2 + 4w^2}{u^2 + 3v^2 + 4w^2} \cdot \frac{F_{NPP}}{F_{NPPref}} \quad (22)$$

Values of *v* and *w* are randomly sampled from the range suggested for the modern ocean (Table S2). We chose different ranges of *v* for different classes of zooplankton in the model (small and large; Table S2).

The typical aggregate velocity, *u*, for the modern ocean is a wide range and has been found to exhibit a bimodal distribution, with substantial values around 1 m d^{-1}, and close to 1000 m d^{-1}, but very few aggregates with settling velocities between these values[22,23]. The *u* in our model takes values between 10 and 1000 m d^{-1} and is truncated to this range for aggregates that fall above/below these values. The value of E_{total} is between 0 and 1, and if its value in rare cases (e.g. higher calculated aggregate velocity, u_i, than the typical value, *u*) exceeds 1, the value of E_{total} is set to 1. The calculated encounter rate is then be compared to a randomly generated value, *r*, and if $r < E_{total}$, the zooplankton encounter and either ingest or fragment the aggregate.

4.2. Fragmentation

To determine whether the aggregates encountered by zooplankton are fragmented or ingested, our model first evaluates the chance of fragmentation. Assuming that the probability of breaking larger particles is higher than that of smaller ones, the parameter R_{break} increases as the aggregate radius increases. Similar to previous work, we define R_{break} as[1]:

$$R_{break} = 0.1 \tan^{-1}({}^{r_a}/_{10^4}) \quad (23)$$

where r_a is the aggregate radius, as described above. If a randomly generated value, *r*, is smaller than $<R_{break}$, the aggregate fragments into a number of daughter particles. Following previous work[1] we use a power law with support between 2 and 24 integers (fragments) that describes the number of fragments, *f*, an aggregate can fragment into (2):

$$P_f = \sum_{i=2}^{f} 0.91.\, i^{-1.56} \quad . \tag{24}$$

A randomly generated value, *r*, is compared to the value of P_f for each successive *f* starting from 2. When $r < P_f$, the number of fragments that the aggregate breaks into is obtained. The radius of the fragmented aggregate is then calculated by dividing the old radius by the number of fragments, *f*.

Recent observation indicates a depth variation in the efficiency of particle fragmentation by zooplankton, with elevated fragmentation in shallower parts of ocean mesopelagic zone and attenuated fragmentation in deeper parts. To account for such variation in efficiency of fragmentation, we multiplied the R_{break} with a power-law function ($f_{frag} = k_{frag} \,.\, z^{-0.258}$; where k_{frag} is between 0.1-1) that mimics the observed depth profile of fragmentation rate with maximum value of 1 at 200m[14].

Within zooplankton community, not all of the zooplankton have the same efficiency in fragmentating oceanic aggregates, and there are even some species that are ingesting oceanic aggregates and produce fecal pellet but are not fragmentating the aggregates (e.g., salps; ref). To take into account such variation in efficiency of particle fragmentation and absence of fragmentation for some zooplankton we changed the value of k_{frag} between 0.1 and 1.

4.3. Ingestion

If the particle is not fragmented, it is ingested and can produce faecal fpellets. To assure that zooplankton do not ingest aggregates without organic matter, a randomly generated value, *r*, is compared to the organic weight fraction (f_{org}) in each aggregate and if $r < f_{org}$, the aggregate is considered to be ingestible. Ingestion of aggregates by zooplankton results in a range of faecal pellet sizes. Faecal pellets are treated by the model essentially as aggregates with much lower porosity, between 43 – 50% [24](Table S2). The size of faecal pellets produced in any single interaction is determined through random selection assuming uniform distribution. The range of values for faecal pellet size are obtained from the relationship between mean faecal pellet volume and prosome length for copepods[25]:

$$log\ PV = 2.58\ log\ PL - 2.38 \tag{25}$$

where *PV* and *PL* represent the pellet volume and prosome length respectively. To account for a range of sizes in different zooplankton classes (small vs large), we assume ranges of prosome lengths (Table S2).

Effect of Diel Vertical Migration (DVM)

To explore the effect of DVM on POC, we assumed that a portion of the produced organic matter in the epipelagic zone would be transferred into mesopelagic zone by zooplankton through DVM, which would reduce the available organic matter at the surface, while transferring the fresh organic matter into deeper parts. The total amount of organic carbon in the mesopelagic zone can be expressed as:

$C_{total} = C_{DVM} + C_{NDVM}$,

where C_{DVM}, and C_{NDVM} are respectively the amount of organic transferred through DVM and the amount of organic transferred through sinking flux not influenced by DVM. The C_{DVM} is also estimated as the concentration of POC at the surface multiplied by a factor, K_{DVM}, that donates the percentage of organic matter content at the surface that is transferred through DVM. Its value was considered to be between 5-40%, and the range of depth within which organic matter is transferred through DVM is considered to be between 300-800 meter. While relatively simple, this parameterization allows us to investigate the effect of evolution of large zooplankton with ability to conduct DVM on the POC flux, transfer efficiency, and oxygen dynamics in the ocean.

5. Transfer efficiency and rate of organic carbon degradation

The average velocity of sinking aggregates at each depth can be used to calculate the age of organic particles at each depth layer:

$$t_{age} = \frac{z_i}{u_{i,average}} \quad , \quad (26)$$

where z_i is a given depth (m) and $u_{i,\ average}$ is the average velocity of aggregates at depth i - (m/day). Having obtained the average age-depth profile, the organic matter content in aggregates is then re-calculated using age-dependent power law, described by Middelburg (1989)[26]:

$$R = -bt^{-a}C, \quad (27)$$

where C is the concentration of organic matter and the constants a and b define the rate of organic carbon mineralization. The Middelburg power law has been found to hold over a wide range of organic matter degradation timescales, ranging from fresh phytoplankton to sedimentary organic matter buried millions of years ago[26].

However, this relationship does not account for the effect of temperature, dissolved oxygen concentrations, mineral matrix properties, or other factors that likely also impact rates of carbon degradation[27–29]. In particular, differences between organic carbon reactivities in oxic versus anoxic conditions[30] strongly influence the efficiency of carbon burial on geological time scales[27,31]. To explore the effect of oxygen on the ocean carbon pump, we employ a modified power law[32] in which the reactivity of organic matter in oxic vs anoxic settings is distinguished through incorporating different a and b values into the Middleburg power law[32].

While this power law accounts for the effect of dissolved oxygen, similar to the Middleburg power law, it does not explicitly include any dependency on seawater temperature. To overcome this issue we further modified the power law carbon degradation rate, following [2,33,34], by adding

a temperature dependency factor, Q_{10}, which for most biological systems is somewhere between 1.5 and 2.5[33,34]:

$$R = Q_{10}^{\frac{T-T_{ref}}{10}} . -bt^{-a}C \quad (28)$$

where T_{ref} is a reference temperature. With a profile for organic matter and sinking rate recalculated, the transfer efficiency of biological carbon pump is calculated as C/C_0, where C_0 is the organic carbon amount at the top of our domain and C is the amount that buried in the deep sediment.

5.1. Effect of transfer efficiency of sediment

While our model calculates the fraction of organic matter produced in the water column and buried in the sediment, a fraction of the organic matter delivered by the water column would be degraded by aerobic and anaerobic respiration during early diagenesis. To account for the effect of sediment on total transfer efficiency of carbon in the ocean, we multiply the transfer efficiency of carbon in the water column to the burial efficiency of carbon in the sediment. The total burial efficiency can then be expressed as:

$$BE = BE_{sed} . TE_{water}, \quad (29)$$

Where BE_{sed} is the burial efficiency of sediment and TE_{water} donates the transfer efficiency resulted from our water column model. The range of BE_{sed} is further parametrized into the sum of transfer efficiency of deep and coastal sediments that are corrected to account for the significance of organic burial in coastal vs deep settings. The BE_{sed} is then parameterized as:

$$BE_{sed} = f_{coast} * BE_{sed\text{-}coast} + f_{deep} * BE_{sed\text{-}deep.} \quad (30)$$

Here $BE_{sed\text{-}coast}$, and $BE_{sed\text{-}deep}$, respectively, denote the efficiency of carbon burial in the coastal and deep ocean settings. The coefficients f_{coast}, and f_{deep} represent the contribution of coastal vs deep settings in the overall transfer efficiency of ocean sediments ($f_{coast} + f_{deep} = 1$). We opted values more than 0.5 for f_{coast}, consistent with the substantial contribution of coastal settling in burying organic matter.

5.2. Calculation of Total Organic Carbon (TOC)

To compare the results from our model against the measured organic content in the sedimentary rock record we further calculate the range of total organic carbon (TOC) that are buried in the sediments. The TOC can be calculated using the net primary production (NPP), the modelled transfer efficiency that is corrected for sediment transfer efficiency, burial velocity, porosity, and the density of solid particles:

$$TOC = (BE . k_{prod} . NPP . \varphi) / (V_{burial} . (1-\varphi) . \rho) \quad (31)$$

Here *BE, NPP*, φ, $V_{burial,}$ ρ , respectively, denote the corrected transfer efficiency described in the previous section, modern net primary production, porosity, burial velocity in the sediment, and density of sediment. The NPP values during Precambrian was most likely lower than that of in the modern ocean [35,36], and consider this difference we defined a factor k_{prod}, named productivity factor, with values less than 1. Finally, given the uncertainty involved in choice of each parameter in estimating the TOC in each major geological time, we employed a stochastic approach, wherein the value for each parameter described above would be randomly selected from a reasonable range assuming a uniform distribution and the most statistically probable range of TOC would be obtained. The range of parameters used in the stochastic calculation of TOC is presented in Table S2. The obtained range is then compared against the range of measured TOC in the rock records during major times of Archean, Proterozoic, and Phanerozoic. The result for TOC comparison is presented in the Fig. S2. Despite the considerable error bar for the measured TOC in the rock records, the average values for modelled TOC and measured ones are consistent. The results also indicate that there is no correlation between the amount of organic matter preserved in the rock records and strength of net primary production. For instance, during the Archean, low net primary production caused by strong nutrient limitation (e.g., P) and pervasive iron-rich condition did not necessary translate into small TOC content, as the efficiency of carbon burial was much higher than today, owing to inefficient degradation of carbon under anoxic condition. Emergence of oxic shallow waters in the aftermath of GOE would have enhanced the rate of carbon degradation, resulting in a less efficient (low BE) carbon pump, consistent with relatively lower organic matter content in the Proterozoic rocks, despite an increase in the overall primary production in the Proterozoic oceans[35].

6. Oxygen dynamics

6.1. 1D reaction transport model

To investigate the effect of environmental and biological factors on the oxygen penetration depth in the ocean, we use a one-dimensional steady-state diffusion-advection model. Specifically, we obtain the depth profile for oxygen and dissolved inorganic carbon (DIC) by resolving the following ordinary differential equation at steady state:

$$0 = \frac{d}{dz}\left[K_z \frac{d\,C}{dz} - C(z)v(z)\right] \pm R \quad . \tag{32}$$

Here z is depth below the photic zone, C is the concentration of the compound of interest, K_z is the turbulent diffusion coefficient, $v(z)$ is the advection velocity, and R represents the rate(s) of reaction(s) that consume or produce a given species. The value of the turbulent diffusion is assumed to be relatively high above the chemocline to reflect the highly convective Ekman layer in the upper ocean, linearly decreases to lower value in the thermocline to reflect the high impediment to vertical mixing caused by strong temperature stratification, and then linearly increases to higher values in the deep ocean where the absence of strong temperature gradient permits more effective vertical mixing. The advection coefficient is estimated by dividing the high latitude to deep exchange flux (~50 Sv; 1 Sv = 10^6 m^3/s) by the lateral (cross-sectional) area

of the deep ocean. Due to uncertainty involved with this estimation, the advection term is multiplied by a fitting parameter, α. Values of diffusion coefficients at the surface, thermocline, and the deep oceans along with the fitting parameter for advection term, α, were obtained through providing a rough fit against the measured DIC and oxygen depth profiles in the modern oceans [37] (Fig. 1).

For oxygen, the consumption rates include the rates of aerobic respiration and iron oxidation in the anoxic water column. The rate of oxygen consumption by aerobic respiration was simulated using the Michaelis-Menten kinetics:

$$R_{resp} = R_C \frac{[O_2]}{K_i + [O_2]} \quad . \tag{33}$$

Here, constant K_i, is the half saturation constant that describes the affinity of enzymes for substrate. R_C is the carbon mineralization rate, approximated as $R_C = k\,[OC]$ where the reactivity k was described by the Middelburg power law as a function of carbon age *t:* $\log_{10} k = -0.95 * \log_{10} t - 0.81$. The age in the model is calculated using eq. (26). The organic matter content, *[OC]*, was estimated by dividing the net primary production to the average velocity resulted from the aggregate model. The rate of iron oxidation is assumed to follow first order kinetics:

$$R_{Fe} = k_{fe}\,[O_2]\,[Fe^{2+}] \quad . \tag{34}$$

For simplicity, the concentration of Fe^{2+} (in μM) is set to zero in the oxic zone and increases below the oxygen penetration depth (OPD) as:

$$[Fe^{2+}] = [Fe]_1 \sqrt{z - OPD} \tag{35}$$

where depth $z > OPD$ is in "m" and $[Fe]_1$ is a constant. This mimics typical Fe^{2+} profiles in the sub-oxic zones of the modern freshwater and marine sediments and stratified water columns[38,39]. The OPD is defined as depth where oxygen level becomes less than 0.5 μM. Fig. 1 illustrates the results from the aggregate model coupled to the one dimensional diffusion-advection model for the depth profiles of the rate of organic matter degradation, R_c, oxygen, DIC, and iron (Fe^{2+}) at 10 percent of the modern net primary production (0.1* F_{NPP}), and a seawater oxygen concentration of 2.5 μM [which translates to ~1% of the present atmospheric level (PAL)], with no eukaryotic algae, consistent with the prevailing environmental conditions suggested for most of the Proterozoic.

6.2. Effect of biological mixing within the upper ocean

In addition to the mixing caused by turbulence and advection, evolution of swimming animals (nekton) can influence the mixing structure of the ocean. While our knowledge on the effect of biology in the physical mixing of the ocean is being pieced together, swimming animals can impact the physical structure of the ocean through generating turbulence or transporting fluid through the drift mechanism.

Fluid dynamics can be described as being turbulent or non-turbulent. A Reynolds number, a dimensionless quantity, ($Re = UL/\nu$; eq. 14) is typically used to predict flow patterns. At low Reynolds numbers, there is likely to be non-turbulent, laminar flow, while at high Reynolds numbers there is likely to be turbulent flow. For nekton, speed (U) and length-scale (L) are, respectively, the average swimming speed and body length; whereas, the kinematic viscosity (ν) correspond to the properties of the fluid in which the animal swims. By comparing inertial forces to viscous forces in a fluid and, the Reynolds number determines the balance between inertial and viscous force for a certain fluid. The large Re numbers, then, suggest that inertial forces are dominant; whereas, the small Re numbers implies the dominance of viscous forces. In the case of swimming animals, considering the same fluid properties for all animals (constant ν), larger-sized animals with higher velocity will possess a larger Re numbers than small animals with low swimming velocity. This means if there is a biology-driven turbulence, the turbulence caused by large-sized animals such as whales are more considerable than the turbulence promoted by smaller-sized animals such abundant zooplankton like copepods. Such turbulence can be caused by both horizontally and vertically moving nekton. Specifically, vertical movement of zooplankton through DVM has a potential to disrupt the density gradient in the fluid, with some impacts on the turbulent dissipation rate (ε).

While estimates indicate a potentially important role of swimming animals in influencing the turbulence, empirical (microstructure) measurements in the modern ocean do not support the idea of significant role of biogenic mixing on turbulence[40,41]. More precisely, the earlier estimates predicted that swimming marine organisms with large Re numbers can produce as much kinetic energy as deep-ocean tide- and wind-driven internal waves[42,43]. These estimates show that relatively high turbulence dissipation rate ($\varepsilon = 10^{-5}$ W kg^{-1}) can be generated by aggregation of small animals such as krill (0.01 m) or other cetaceans, which is comparable to energy produced by wind near the surface. As noted above, however, the microstructure measurements have not been able to confirm this prediction; there is no evidence for consistently enhanced turbulent dissipation rate caused by vertically migrating organisms[44–46]. This questions the earlier predictions about the role of biogenic processes on oceanic mixing.

Another term to describe the efficacy of the biologically driven process in modulating the mixing structure of ocean is “mixing efficiency” that measures the ability of a mixing process to translate the available kinetic energy available into the change in the potential energy state of the fluid. The efficiency of biogenic turbulence is controlled by both fluid properties and stratification and the strength of turbulence generated by nekton. For smaller-sized, more abundant animals such as copepods, the mixing efficiency is several orders of magnitude lower than that of produced by larger but less abundant animals such as whales. Given most animal biomass is dominated by small nekton with low mixing efficiencies [47].

Beside turbulence, the swimming animals can influence the mixing structure of the ocean through a mechanism called “drift’’ which does not require a high-speed animal with large sized body to be effective. Briefly, drift occurs when an organism moves through the water and the water around its body is moving as a result of its body pressure. The efficiency of this process in changing the density gradient depends on the shape of the body and its swimming direction with respect to the fluid. To influence density stratification, effective drift can be produced by vertically migrating organisms, suggesting the role of DVM as a main source for generating

considerable ‘’drift’’. This low-Reynold-number mechanism, however, was suggested to be ineffective when factors such as swimming behaviour and molecular scalar diffusion considered[44,46,48].

While uncertainty in quantifying the effect of biogenic mixing exists, we explored the effect of enhanced mixing by evolution of larger animals (e.g., cetaceans) and vertically migrating animals by increasing the values of turbulent (eddy) diffusion coefficient (K_z) in epipelagic and mesopelagic zones, where the significant effect of biological mixing is likely. The results for the effect of increased K_z in the surface waters is presented in Fig. S3. We performed our simulation for atmospheric oxygen level of 25% and 10% (PAL), as the evolution of large swimming animals would have occurred under relatively well-oxygenated condition. While our results show an important role of mixing kinetics (K_z) in controlling the shape of oxygen depth profile, it does not have significant impact on the transfer efficiency of carbon nor the flux of POC in the ocean.

6.3. Effect of filter-feeding benthos

By processing the water that include particulate organic matter, filter-feeding organism can influence the POC concentration with consequence on ocean ventilation. Effect of filter-feeding organism have been shown to be important in the modern restricted shallow water settings [49]. Mechanistically, filter-feeding organism through aerobic metabolism can uptake small organic cells (< 10 μm diameter) as well as small sized particulate organic matter[50], decreasing the POC concentration in the water with impact on clarity of the water and light penetration depth. The significance of this effect on the global POC flux, however, remains to be constrained.

While the timing for the evolution and ecological dominance of the filter-feeding organism are not well constrained, the later Neoproterozoic ocean is suggested to have hosted such organisms. Despite the low-oxygen requirement (~1% PAL) for some filter-feeding organisms (e.g., sponges), their ecological significance and their body size would be hampered at low oxygen levels[51].

Whenever the filter-feeding evolved in the ocean, there could have had some effect on the POC concentration in the open ocean as well. To explore the effect that this mechanism could have had on oxygen dynamic and POC flux, we further parameterized the equations for solving the steady-state oxygen concentration in the ocean. Specifically, we assumed a fraction of POC produced in the photic zone can be up-taken through filter feeding, decreasing the POC concentration while increasing the demand for oxygen in the ocean. The amount of POC processed through filter-feeding can then be expressed as:

$$C_{total\_filter} = (K_{filter}) * C_{total}, \quad (36)$$

Where C_{total_filter}, K_{filter}, and C_{total} are, respectively, the total amount of organic in the presence of filter-feeding, the fraction of total POC processed by filter-feeding, and the total amount of organic without filter-feeding. The rate of oxygen consumption through filter-feeding can also be written similar to the aerobic respiration (eq. 33) using different half-saturation constant:

$$R_{resp\_filter} = k_{filter} R_C \frac{[O_2]}{K_{sat\_filter}+[O_2]}$$
(37)

The parameters are similar to the parameters described for the equation (33), except there is a coefficient for the fraction of organic channelled through filter-feeding (K_{filter}), and also the half-saturation constant for this metabolism is higher than that of suggested for aerobic heterotrophy. We used the maximum value of 0.2 for K_{filter}, meaning 20% of the POC would be used by filter-feeding, which might be an overestimation for the effect that this process would have on the oceanic POC concentration. Our results using this value indicate an unimportant role of filter-feeding in efficiency of carbon pump as well as the oxygen dynamic (Fig. S4). While an increase in POC removal caused by filter-feeding can elevate the oxygen availability, due to oxygen consumption during this process, the net effect on the oxygen dynamic in the ocean is small relatively to other environmental and biotic factors (Fig. S4).

7. Phosphorous cycling and primary productivity

Based on the power law of organic matter degradation, higher rates of organic matter degradation under oxic conditions result in an enhancement in phosphorous release from organic matter, leading to an increase in the availability of phosphorous in the surface layers. Similarly, slow sinking rates should lead to P accumulation in the surface oceans and higher primary productivity. In contrast, anoxia leads to lower rates of organic matter degradation, decrease in P release from organic matter, and less efficient P recycling[52]. To account for this effect, we revise the productivity factor, K_{produc}.

Assuming the net primary production at any geological time of interest is proportional to the modern net primary production, the net primary production in the past can be defined as:

$$F_{NPP,\ past} = K_{produc} * F_{NPP,\ modern}$$
(38)

where K_{produc} is a dimensionless value between 0 and 1. Net primary production itself can be expressed as:

$$F_{NPP} = \frac{\left(\alpha z_{mix} \varepsilon [PO_4^{3-}] \frac{[PO_4^{3-}]}{[PO_4^{3-}]+k_p}\right)}{f_{ex}}$$
(39)

where the f_{ex} denotes the export ratio (i.e., the ratio of carbon export from the mixed layer relative to net primary productivity), α denotes the C/P stoichiometry of primary producers, z_{max} is the mixed layer depth, ε is the efficiency factor for phosphorus uptake, and k_P is the half-saturation constant for nutrient-limited growth. Defining the K_{produc} as the ratio of net primary productions at two different times, K_{produc} can be rewritten as:

$$K_{produc} = \frac{\left(\alpha_i z_{mix,i} \varepsilon_i [PO_4^{3-}]_i \frac{[PO_4^{3-}]_i}{[PO_4^{3-}]_i + k_{p,i}}\right)}{\left(\alpha_j z_{mix,j} \varepsilon_j [PO_4^{3-}]_j \frac{[PO_4^{3-}]_j}{[PO_4^{3-}]_j + k_{p,i}}\right)} \frac{f_{ex_i}}{f_{ex_j}}$$

(40)

where subscripts *i* and *j*, respectively, correspond to the past geologic time and the modern state. Assuming a constant z_{max}, ε, and k_P through time, the productivity factor, K_{produc}, is dependent only on seawater phosphate concentration, C/P stoichiometry, α, and export ratio, f_{ex}. Given the low suggested value for k_P (1 nM), and the suggested range of phosphate concentration through geological time (0.1 to 3 μM) the last term in the equation can be set to 1. The equation then simplifies to:

$$K_{produc} = \frac{\left(\alpha_i [PO_4^{3-}]_i\right)}{\left(\alpha_j [PO_4^{3-}]_j\right)} \frac{f_{ex_i}}{f_{ex_j}} \quad .$$

(41)

Phosphate availability in the photic zone is mainly controlled by the weathering input flux of apatite, the efficiency of P recycling in the water column, and the extent of scavenging by reduced iron species in anoxic iron rich oceans [53]d. Taking these factors into account, the ratio of phosphate concentration in the past and modern oceans can be parameterized as:

$$\frac{[PO_4^{3-}]_i}{[PO_4^{3-}]_j} = \frac{J_{p,i}}{J_{p,j}} \tau_{scav} \frac{\int_0^l R_{c,i}}{\int_0^l R_{c,j}} \quad .$$

(42)

Here J_p is the weathering flux of phosphorous at time *i* and *j*, described above, τ_{scav}, is the iron scavenging factor which is between 0 and 1, where 0 correspond to fully oxic condition and 1 represent fully reducing iron rich water column. The last term reflects the efficiency of phosphorous recycling as linked to the ratios of integrated rates of organic matter degradation over the water column. Therefore, the productivity factor, K_{produc} is defined as:

$$K_{product} = \frac{\alpha_i}{\alpha_j} \frac{J_{p,i}}{J_{p,j}} \tau_{scav} \frac{\int_0^l R_{c,i}}{\int_0^l R_{c,j}} \frac{f_{ex_i}}{f_{ex_j}} \quad .$$

(43)

In the model, the oxygen penetration depth is first calculated using an assumed productivity factor (K_{produc}), and Middleburg power law, after which the calculated OPD is used to recalculate the K_{produc} using the new calculated rate of organic matter degradation.

8. Sensitivity analysis

To investigate the sensitivity of our results to the values of model parameters, we conducted a sensitivity analysis. Model parameters were varied within their reasonable ranges (specified in Table S2), and changes in transfer efficiency and sinking rates of aggregates at the bottom of the ocean (4000 m) between maximum and minimum of each parameter were recorded. To account for the change in transfer efficiency in different oceanic settings (e.g. continental shelf, coastal, intermediate, and deep oceans), we also report the transfer efficiency at different depths (Fig. S6).

Results from the sensitivity analysis indicate a good correspondence between the distributions of aggregate sinking velocity predicted in our model and those observed in modern marine environments. In particular, observations of particle sinking rates show a bimodal distribution, with significant values of sinking rates around 1 m d^{-1} as well as 1000 m d^{-1}, yet with very little in between these two values, indicating two very different types of marine aggregate are produced in natural systems[22,23]. Results from our model under roughly modern conditions exhibit a strong bimodality, consistent with observations from the modern oceans (Fig. S7). Our modeling result for the sinking rate of aggregates in absence of zooplankton and faecal pellet suggest that prior to the evolution of zooplankton, marine aggregate would have a settling rate between 1 and >100 meters per day, with a central mode at around 1 m d^{-1} (Fig. S7). Our results are apparently in line with the observation of two different types of marine aggregates, but also suggest that such a bimodal distribution is a unique feature that must have emerged in the wake of macro-zooplankton evolution in early Palaeozoic (likely 550-500 million years ago).

Results from the sensitivity analysis also indicate that our primary conclusions are essentially insensitive (<10% relative change in transfer efficiency) to most parameters including change in cell size, net primary production (NPP), fractal dimension (D_N), mixing depth, depth scale for thermocline, aggregation efficiency factor (K_{aggr}), prosome length of zooplankton, and seawater surface density (Fig. S8). The parameters that most strongly impact the efficiency of the biological carbon pump are seawater surface temperature, changes in atmospheric oxygen level (as discussed in the main text), the temperature dependency factor (Q_{10}), and the assumed reference temperature (T_{ref}) (Fig. S8). Specifically, the shift from an oxygen-free atmosphere to one with ~1% of the modern atmospheric oxygen level changes the transfer efficiency by more than 20% (not shown). A sharp decrease in transfer efficiency, resulting from deeper oxygen penetration depth, is consistent with some observations in modern marine and lake sediments where transfer efficiency of organic matter is found to be strongly attenuated at higher oxygen exposure time (OET) - the length of time organic matter is exposed to molecular oxygen in sediment pore waters[29,32,54].

While our results indicate that evolution of both larger-sized algae and non-migrating zooplankton might have not had a significant impact on the efficiency of carbon pump, the evolution of migrating zooplankton would enhance the efficiency of carbon pump (Fig. S9). Specifically, by translocating the fixed carbon from surface waters into depths, through DVM process, vertically migrating zooplankton would enhance the amount of carbon in the ocean interior, resulting in a higher amount of organic matter buried in the deep sediment. While the effect of DVM depends on the depth within which the DVM is active as well as the amount of organic matter transferred into depths, the evolution of migrating zooplankton can lead up to 45% increase in the efficiency of carbon pump (Fig. S9 & S10). Assuming an insignificant effect of DVM in enhancing the physical mixing, by enhancing the POC flux in the mid-water, the evolution of migrating zooplankton would have fostered mid-water anoxia as well (Fig. S9). Low oxygen condition would have decreased the rate of organic matter degradation, which in turn, would lead to an increase in the amount of organic buried in the seafloor (higher transfer efficiency) (Fig. S9).

Despite the large effect of migrating zooplankton on POC flux, relative to other biotic factor, this effect is still less significant than the effects of atmospheric oxygen and seawater surface temperature (Fig. S10 & S11). The degree to which temperature would influence the POC flux and transfer efficiency of carbon pump is heavily dependent upon the choice of Q_{10} (Fig. S8 & S12), which is a measure of temperature sensitivity of organic matter remineralization. Factors such as physiological adaption, selective pressure, and reaction path play an important role in temperature sensitivity[55–60]. Increased reference temperature, on the other hand, results in lower sensitivity of carbon degradation rate at higher temperature, which would result in an increase in the efficiency of the ocean carbon pump.

Our results also reveal that the oxygen penetration depth (OPD) in the ocean is mainly controlled by atmospheric oxygen level as well as seawater surface temperature. Notably, while the change in cell size and evolution of small and large zooplankton do not exert a major control on oxygen penetration depth (Fig. S10), a change in the atmospheric oxygen level can result in a significant shift in oxic-anoxic boundary layer. In addition to atmospheric oxygen level, and temperature, coefficients for physical transports have a strong impact on the OPD. Assuming no change in physical transports of the ocean through time, the OPD in the ocean would have, then, likely be impacted only by environmental drivers rather than change in biological structure of the ocean (Fig. S10 & S11).

The fractal dimension, aggregation efficiency factor, ratio of picoplankton flux to algae flux, ratio of dust flux to organic flux, and, most notably, prosome length of zooplankton are the most important parameters in controlling sinking rates of aggregates in the ocean (Fig. S13). Mixing depth, depth scale for the thermocline, reference temperature, seawater surface density, and oxic depth in the ocean do not significantly affect the sinking rate of oceanic aggregates (<20 m/day change in sinking rate of aggregates). Increased sinking rate of aggregates would enhance the reactivity of organic matter delivered to depths by decreasing the age of organic matter (Eq. 26), but this change in organic matter age is not large enough to significantly affect the rate of organic matter degradation, described by the age-dependent power law function[32].

References:

1. Jokulsdottir, T. & Archer, D. A stochastic, Lagrangian model of sinking biogenic aggregates in the ocean (SLAMS 1.0): Model formulation, validation and sensitivity. *Geosci. Model Dev.* **9**, 1455–1476 (2016).

2. Cram, J. A. *et al.* The Role of Particle Size, Ballast, Temperature, and Oxygen in the Sinking Flux to the Deep Sea. *Global Biogeochem. Cycles* **32**, 858–876 (2018).

3. Riebesell, U. & Wolf-Gladrow, D. A. The relationship between physical aggregation of phytoplankton and particle flux: a numerical model. *Deep Sea Res. Part A, Oceanogr. Res. Pap.* **39**, 1085–1102 (1992).

4. Martin, J. H., Knauer, G. A. & Broenkow, W. W. VERTEX: the lateral transport of manganese in the northeast Pacific. *Deep Sea Res. Part A, Oceanogr. Res. Pap.* **32**, (1985).

5. Burd, A. & Jackson, G. A. Predicting particle coagulation and sedimentation rates for a pulsed input. *J. Geophys. Res. Ocean.* **102**, 10545–10561 (1997).

6. Burd, A. B. & Jackson, G. A. Particle Aggregation. *Ann. Rev. Mar. Sci.* **1**, 65–90 (2009).

7. Li, X. & Logan, B. E. Size distributions and fractal properties of particles during a simulated phytoplankton bloom in a mesocosm. *Deep. Res. Part II* **42**, 125–138 (1995).

8. Logan, B. E. & Wilkinson, D. B. Fractal geometry of marine snow and other biological aggregates. *Limnology and Oceanography* **35**, 130–136 (1990).

9. Trull, T. W. *et al.* In situ measurement of mesopelagic particle sinking rates and the control of carbon transfer to the ocean interior during the Vertical Flux in the Global Ocean (VERTIGO) voyages in the North Pacific. *Deep. Res. Part II Top. Stud. Oceanogr.* **55**, 1684–1695 (2008).

10. Berelson, W. M. Particle settling rates increase with depth in the ocean. *Deep. Res. Part II Top. Stud. Oceanogr.* **49**, 237–251 (2001).

11. Alldredge, A. L., Granata, T. C., Gotschalk, C. C. & Dickey, T. D. The physical strength of marine snow and its implications for particle disaggregation in the ocean. *Limnol. Oceanogr.* **35**, 1415–1428 (1990).

12. awawda, lama. Fluid Mechanics Frank White 5th Ed.

13. Dorsey, N. E. (Noah E. & 1873, b. Properties of ordinary water-substance in all its phases. (1940).

14. Briggs, N., Dall'olmo, G. & Claustre, H. Major role of particle fragmentation in regulating biological sequestration of CO 2 by the oceans Downloaded from. (2020). doi:10.17882/70484

15. Dilling, L. & Alldredge, A. L. Fragmentation of marine snow by swimming macrozooplankton: A new process impacting carbon cycling in the sea. *Deep. Res. Part I Oceanogr. Res. Pap.* **47**, 1227–1245 (2000).

16. Iversen, M. H. *et al.* Sinkers or floaters? Contribution from salp pellets to the export flux during a large bloom event in the Southern Ocean. *Deep. Res. Part II Top. Stud. Oceanogr.* **138**, 116–125 (2017).

17. H. Cohen, J. & B. Forward Jr, R. Zooplankton Diel Vertical Migration ,Äî A Review Of Proximate Control. in 77–109 (2009). doi:10.1201/9781420094220.ch2

18. Bianchi, D., Galbraith, E. D., Carozza, D. A., Mislan, K. A. S. & Stock, C. A. Intensification of

open-ocean oxygen depletion by vertically migrating animals. *Nat. Geosci.* **6**, 545–548 (2013).

19. Bollens, S. M., Rollwagen-Bollens, G., Quenette, J. A. & Bochdansky, A. B. Cascading migrations and implications for vertical fluxes in pelagic ecosystems. *J. Plankton Res.* **33**, 349–355 (2011).

20. Dzierzbicka-Głowacka, L. Encounter rates in zooplankton. *Polish J. Environ. Stud.* **15**, 243–257 (2006).

21. Kiørboe, T. & Mackenzie, B. Turbulence-enhanced prey encounter rates in larval fish: Effects of spatial scale, larval behaviour and size. *J. Plankton Res.* **17**, 2319–2331 (1995).

22. Alonso-Gonzalez, I. J. *et al.* Role of slowly settling particles in the ocean carbon cycle. *Geophys. Res. Lett.* **37**, (2010).

23. McDonnell, A. M. P. & Buesseler, K. O. Variability in the average sinking velocity of marine particles. *Limnol. Oceanogr.* **55**, 2085–2096 (2010).

24. Ploug, H., Iversen, M. H. & Fischer, G. Ballast, sinking velocity, and apparent diffusivity within marine snow and zooplankton fecal pellets: Implications for substrate turnover by attached bacteria. *Limnol. Oceanogr.* **53**, 1878–1886 (2008).

25. Uye, S. ichi & Kaname, K. Relations between fecal pellet volume and body size for major zooplankters of the Inland Sea of Japan. *J. Oceanogr.* **50**, 43–49 (1994).

26. Middelburg, J. J. A simple rate model for organic matter decomposition in marine sediments. *Geochim. Cosmochim. Acta* **53**, 1577–1581 (1989).

27. Hedges, J. I. & Keil, R. G. Sedimentary organic matter preservation: an assessment and speculative synthesis. *Marine Chemistry* **49**, 81–115 (1995).

28. Hulthe, G., Hulth, S. & Hall, P. O. J. Effect of oxygen on degradation rate of refractory and labile organic matter in continental margin sediments. *Geochim. Cosmochim. Acta* **62**, 1319–1328 (1998).

29. Burdige, D. J. Preservation of organic matter in marine sediments: Controls, mechanisms, and an imbalance in sediment organic carbon budgets? *Chem. Rev.* **107**, 467–485 (2007).

30. Canfield, D. E. Factors influencing organic carbon preservation in marine sediments. *Chem. Geol.* **114**, 315–329 (1994).

31. Cowie, G. L., Hedges, J. I., Prahl, F. G. & de Lance, G. J. Elemental and major biochemical changes across an oxidation front in a relict turbidite: An oxygen effect. *Geochim. Cosmochim. Acta* **59**, 33–46 (1995).

32. Katsev, S. & Crowe, S. A. Organic carbon burial efficiencies in sediments: The power law of mineralization revisited. *Geology* **43**, (2015).

33. Quinlan, A. V. The Thermal Sensitivity of Michaelis-Menten Kinetics as a Function of Substrate Concentration. *J. Franklin Inst.* **310**, 325–342 (1980).

34. Quinlan, A. V. The thermal sensitivity of generic Michaelis-Menten processes without catalyst denaturation or inhibition. *J. Therm. Biol.* **6**, 103–114 (1981).

35. Crockford, P. W. *et al.* Triple oxygen isotope evidence for limited mid-Proterozoic primary productivity. *Nature* **559**, 613–616 (2018).

36. Laakso, T. A. & Schrag, D. P. A small marine biosphere in the Proterozoic. *Geobiology* **17**, 161–171 (2019).

37. Dore, J. E., Lukas, R., Sadler, D. W., Church, M. J. & Karl, D. M. Physical and biogeochemical modulation of ocean acidification in the central North Pacific. *Proc. Natl. Acad. Sci. U. S. A.* **106**, 12235–12240 (2009).

38. Jorgensen, B. B. & Kasten, S. Sulfur cycling and methane oxidation. in *Marine Geochemistry* 271–309 (Springer Berlin Heidelberg, 2006). doi:10.1007/3-540-32144-6_8

39. Li, J., Zhang, Y. & Katsev, S. Phosphorus recycling in deeply oxygenated sediments in Lake Superior controlled by organic matter mineralization. *Limnol. Oceanogr.* **63**, 1372–1385 (2018).

40. Munk, W. H. *Abyssal recipes*. **13**, (Pergamon Press Ltd, 1966).

41. Dewar, W. K. *et al.* Does the marine biosphere mix the ocean? *J. Mar. Res.* **64**, 541–561 (2006).

42. Simmons, H. L., Hallberg, R. W. & Arbic, B. K. Internal wave generation in a global baroclinic tide model. in *Deep-Sea Research Part II: Topical Studies in Oceanography* **51**, 3043–3068 (Pergamon, 2004).

43. Rimac, A., Storch, J., Eden, C. & Haak, H. The influence of high- resolution wind stress field on the power input to near- inertial motions in the ocean. *Geophys. Res. Lett.* **40**, 4882–4886 (2013).

44. Wagner, G. L., Young, W. R. & Lauga, E. Mixing by microorganisms in stratified fluids. *J. Mar. Res.* **72**, 47–72 (2014).

45. Thiffeault, J. L. & Childress, S. Stirring by swimming bodies. *Phys. Lett. Sect. A Gen. At. Solid State Phys.* **374**, 3487–3490 (2010).

46. Leshansky, A. M. & Pismen, L. M. Do small swimmers mix the ocean? *Phys. Rev. E - Stat. Nonlinear, Soft Matter Phys.* **82**, 025301 (2010).

47. Katija, K. Biogenic inputs to ocean mixing. *J. Exp. Biol.* **215**, 1040–1049 (2012).

48. Kunze, E. Fluid mixing by swimming organisms in the low-Reynolds-number limit. *J. Mar. Res.* **69**, 591–601 (2011).

49. Peterson, B., Chester, C., Jochem, F. & Fourqurean, J. Potential role of sponge communities in controlling phytoplankton blooms in Florida Bay. *Mar. Ecol. Prog. Ser.* **328**, 93–103 (2006).

50. Yahel, G., Sharp, J. H., Marie, D., Häse, C. & Genin, A. In situ feeding and element removal in the symbiont-bearing sponge Theonella swinhoei: Bulk DOC is the major source for carbon. *Limnol. Oceanogr.* **48**, 141–149 (2003).

51. Sperling, E. A., Halverson, G. P., Knoll, A. H., MacDonald, F. A. & Johnston, D. T. A basin redox transect at the dawn of animal life. *Earth Planet. Sci. Lett.* **371**–**372**, 143–155 (2013).

52. Kipp, M. A. & Stüeken, E. E. Biomass recycling and Earth's early phosphorus cycle. *Sci. Adv.* **3**, 1–7 (2017).

53. Reinhard, C. T. *et al.* Evolution of the global phosphorus cycle. *Nature* **541**, 386–389 (2017).

54. Hartnett, H. E., Keil, R. G., Hedges, J. I. & Devol, A. H. Influence of oxygen exposure time on organic carbon preservation in continental margin sediments. *Nature* **391**, 572–574 (1998).

55. Weston, N. B. & Joye, S. B. Temperature-driven decoupling of key phases of organic matter degradation in marine sediments. *Proc. Natl. Acad. Sci. U. S. A.* **102**, 17036–17040 (2005).

56. Arnosti, C., Jørgensen, B. B., Sagemann, J. & Thamdrup, B. Temperature dependence of microbial degradation of organic matter in marine sediments: Polysaccharide hydrolysis, oxygen consumption, and sulfate reduction. *Mar. Ecol. Prog. Ser.* **165**, 59–70 (1998).

57. Thamdrup, B. & Fleischer, S. Temperature dependence of oxygen respiration, nitrogen mineralization, and nitrification in Arctic sediments. *Aquat. Microb. Ecol.* **15**, 191–199 (1998).

58. Ågren, G. I. & Bosatta, E. Reconciling differences in predictions of temperature response of soil organic matter. *Soil Biol. Biochem.* **34**, 129–132 (2002).

59. Kirchman, D. L., Malmstrom, R. R. & Cottrell, M. T. Control of bacterial growth by temperature and organic matter in the Western Arctic. *Deep. Res. Part II Top. Stud. Oceanogr.* **52**, 3386–3395 (2005).

60. Davidson, E. A. & Janssens, I. A. Temperature sensitivity of soil carbon decomposition and feedbacks to climate change. *Nature* **440**, 165–173 (2006).

61. Finkel, Z. V. Marine net primary production. in *Global Environmental Change* 117–124 (Springer Netherlands, 2014). doi:10.1007/978-94-007-5784-4_42

62. Folger, D. W. Desert Dust: Origin, Characteristics, and Effect on Man. *Eos, Trans. Am. Geophys. Union* **64**, 146 (1983).

63. Ozaki, K. & Tajika, E. Biogeochemical effects of atmospheric oxygen concentration, phosphorus weathering, and sea-level stand on oceanic redox chemistry: Implications for greenhouse climates. *Earth Planet. Sci. Lett.* **373**, 129–139 (2013).

64. Katsev, S., Rancourt, D. G. & L'Heureux, I. dSED: A database tool for modeling sediment early diagenesis. *Comput. Geosci.* **30**, 959–967 (2004).

65. Reinhard, C. T. *et al.* Evolution of the global phosphorus cycle. *Nat. Publ. Gr.* **541**, (2017).

66. Ozaki, K., Reinhard, C. T. & Tajika, E. A sluggish mid-Proterozoic biosphere and its effect on Earth's redox balance. *Geobiology* **17**, 3–11 (2019).

67. Laakso, T. A. & Schrag, D. P. A theory of atmospheric oxygen. *Geobiology* **15**, 366–384 (2017).

Table S1. The probability, *P*, for a type of particle to be produced and range of values for different conditions, different types of primary particles with the amount of material in each particle (pmol particl^{-1}) and their densities. Particle types: C is coccolithophorid, A is Aragonite forming phytoplankton, Di is diatom, Pi is picoplankton, D = dust, Ca is calcite.

Type	***P***	**Range**	**OrgC**	**Calcite**	**Aragonite**	**bSi**	**Clay**	**ρ (g cm^{-3})**
C	0.06	0-0.25	7	1.5	0	0	0	1.92
A	0.06	0-0.25	7	0	1.5	0	0	1.92
Di	0.02	0-0.15	15	0	0	5	0	1.24
Pi	0.7	0.3-0.9	1	0	0	0	0	1.06
D	0.15	0.05-0.2	0	0	0	0	2.85	2.65
Ca	0.01	0-0.05	0	2.5	0	0	0	2.55

Table S2. Parameters for stochastic model of sinking rates of aggregates and sensitivity

analysis (SA). Range of transfer efficiency and oxygen penetration depth presented in the figure 2,3, and 5 main text were obtained with changing the input parameters.

Parameter	Symbol	Value	Unit	Range used in the SA
Net primary production flux	F_{NPP}	0.06	gC m^{-2} yr^{-1}	100-400[61]
Dust flux	F_{Dust}	0.04	Pg yr^{-1}	0.01-0.1[62]
Calcite flux	F_{Ca}	0.01	Pg yr^{-1}	0.005-0.05
Silica flux	*Fsilica*	0.005	Pg yr^{-1}	0.001-0.01
Mixing depth	L_{mix}	200	m	200-400
Temperature dependency factor	Q_{10}	1	-	1.2-2.2[33,34]
Depth scale for thermocline	L_{thermo}	800	m	800-1200
Reference temperature	*Tref*	4	^{o} C	4-25
Aggregation efficiency factor	K_{aggr}	0.5	-	0.1-1
Fractal dimension	D_N	2	-	1.3-3[1]
Seawater surface temperature	*SST*	25	^{o} C	4-35
Seawater surface density	*SSD*	1.0255	g/cm^3	1.0253-1.026
Fraction of NPP by picoplankton	f_{Pi}	0.75	-	0.4 - 0.9
Fraction of NPP by coccolithophorid	f_C	0.1	-	0 – 0.3
Fraction of NPP by Aragonite forming phytoplankton	f_A	0.1	-	0 – 0.3
Fraction of NPP by diatom	f_{Di}	0.05	-	0 – 0.15
Stefan– Boltzman constant	k_{Boltz}	1.380 $x10^{-23}$	m^2 kg s^{-2} K^{-1}	
Reference value for collision rate	β_{ref}	$1x10^{-15}$	m^3/s	$1x10^{-15}$- $1x10^{-12}$
Turbulent dissipation rate	ε	1×10^{-4}	m^2/s^3	1×10^{-5} - 1×10^{-31}
Prosome Length (small zooplankton)	*PL*	-	µm	100-500[25]
Prosome Length (large zooplankton)	*PL*	-	µm	300-2000[25]
Turbulent Velocity	*w*	1	m/s	10-25[20]
Zooplankton Velocity (small zooplankton)	*v*	-	m/d	100 - 1000
Zooplankton Velocity (large zooplankton)	*v*	-	m/d	1000 - 6000
Eddy diffusion coefficient at the surface	$K_{z,\,surf}$	5×10^{-3}	m^2/s	10^{-3} - 10^{-2} ([63])
Eddy diffusion coefficient at the thermocline	$K_{z,\,therm}$	6×10^{-4}	m^2/s	10^{-4} - 10^{-3} ([63])
Eddy diffusion coefficient in the deep ocean	$K_{z,\,depp}$	6×10^{-3}	m^2/s	10^{-3} - 10^{-2} ([63])
Monod constant for O_2	K_i	2	μM	1 – 2 [64]
Iron oxidation rate constant	k_{fe}	100	1/µM/year	100-500 [64]
Carbon to Phosphorous ratio	*C/P*	106	mol/mol	106-500
iron scavenging factor	τ_{scav}	0.5	-	0 – 1 [65]
export ratio	f_{ex}	0.2	-	0.2-0.3 [66]

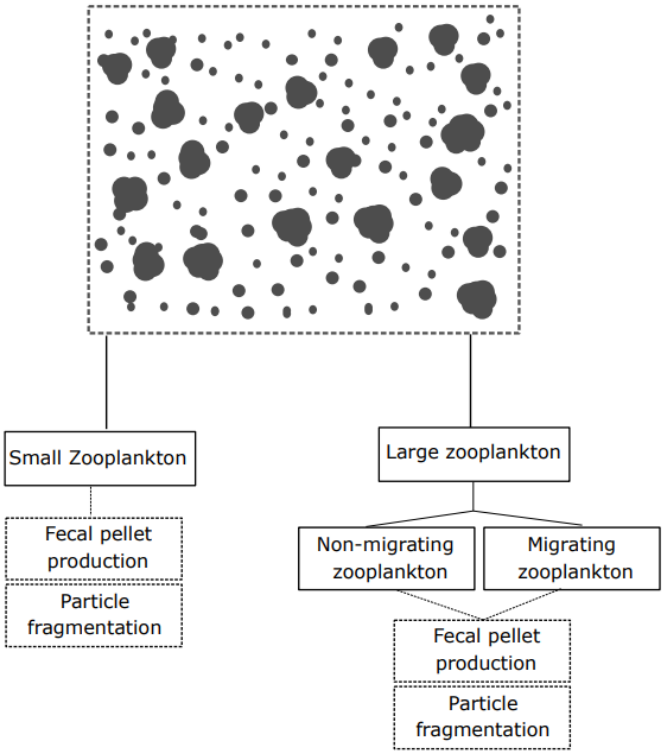

Fig. S1. Zooplankton classes considered in the model. Upon the encountering of zooplankton with oceanic aggregates, depending on the zooplankton class, the particle can be fragmented, ingested and converted into fecal pellet, or transferred vertically into depths by diel vertical migration (DVM). While in the model both zooplankton classes influence the oceanic aggregates by fragmentation, migrating zooplankton can further affect the POC flux through direct transfer of organic material from epipelagic to mesopelagic depths.

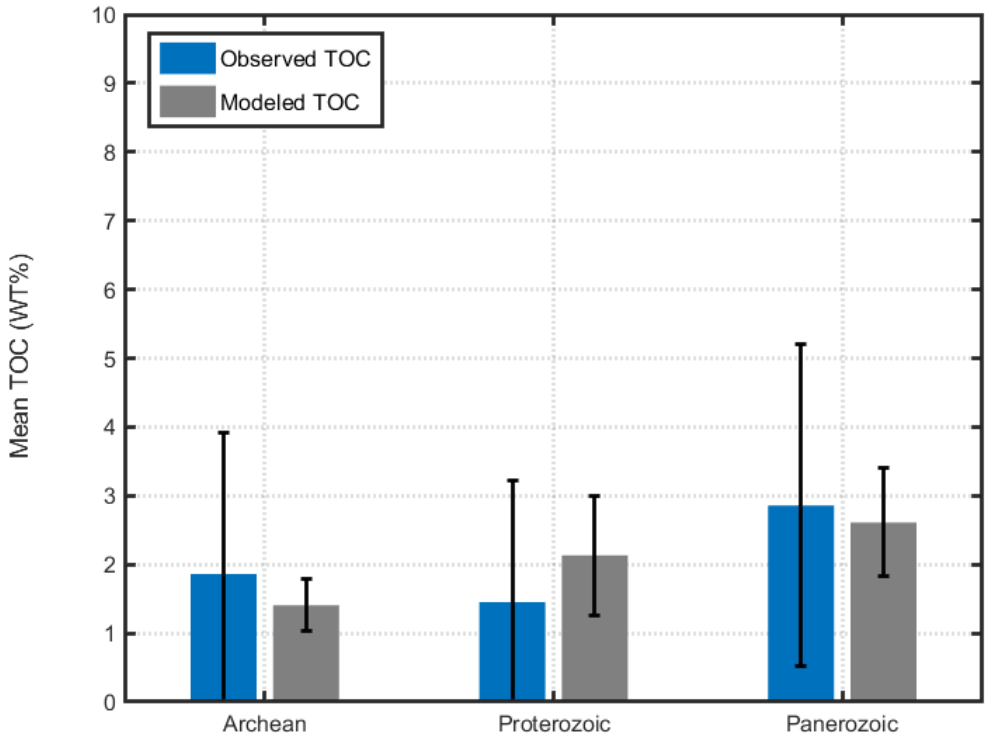

Fig. S2. Modeled TOC compared to measured TOC in Earth's rock record[53]. The range for modeled TOC is calculated using Eq. 31. The results from the model are binned into three major geological time periods (Archean, Proterozoic, and Phanerozoic). While the error bar for the measured TOC is substantially larger than that of from the model, the difference between average values are not statistically distinguishable, suggesting the consistency of the range of transfer efficiency calculated by our model with the observed TOC in the rock record[53].

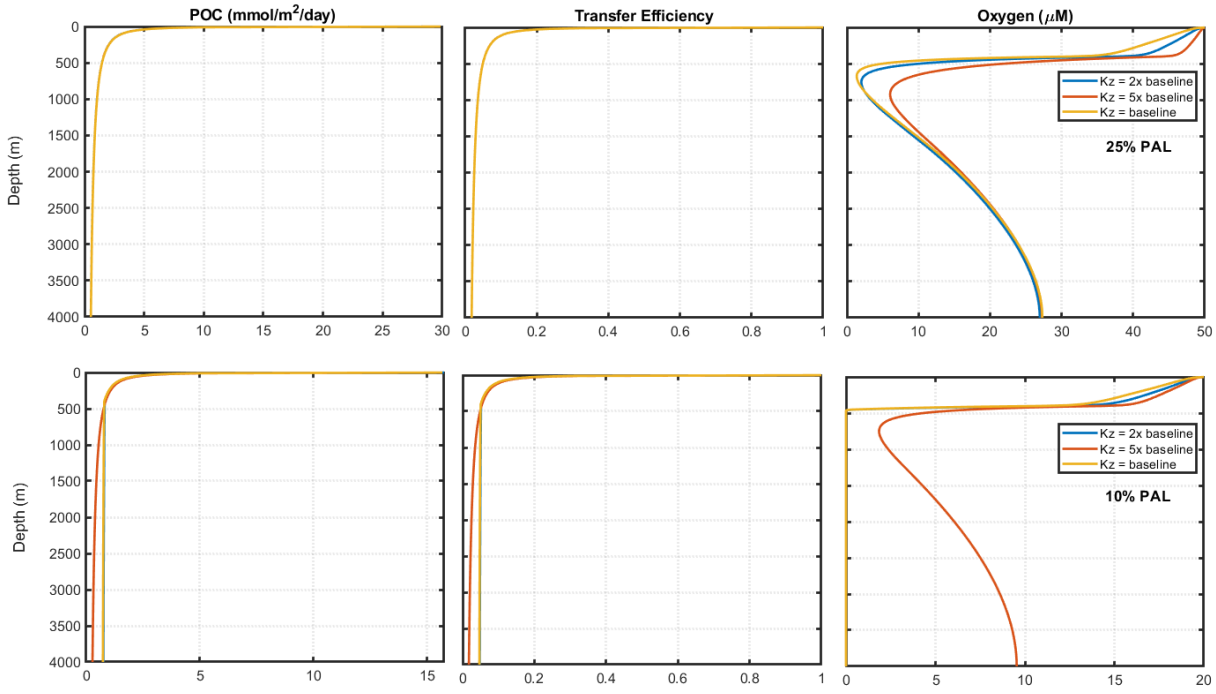

Fig. S3. Effect of increased mixing kinetics on POC flux, transfer efficiency, and water column oxygen distribution at two different atmospheric oxygen levels. While an increase in the mixing kinetics results in higher oxygen concentration at depth and lower chance of anoxia, it does not affect the efficiency of the carbon pump (transfer efficiency) and the overall flux of POC in the ocean. At 10% PAL, increased mixing would enhance ocean oxygenation, resulting in higher organic matter degradation in depth and lower transfer efficiency. Increased mixing kinetics can mimic an increase in the mixing kinetics caused by evolution of large swimming animals.

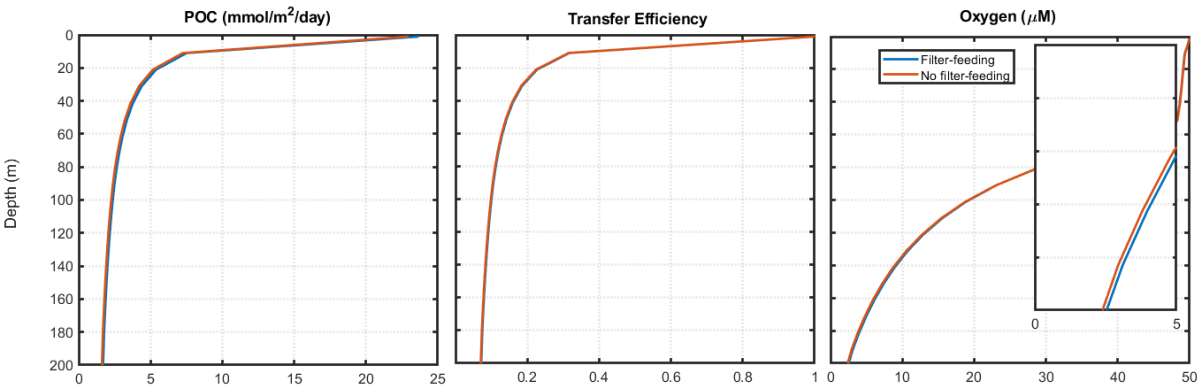

Fig. S4. Effect of filter-feeding on POC flux, transfer efficiency, and oxygen dynamic. Our results indicate an insignificant role of filter-feeding in modulating the depth profiles of POC flux, transfer efficiency, and oxygen concentration.

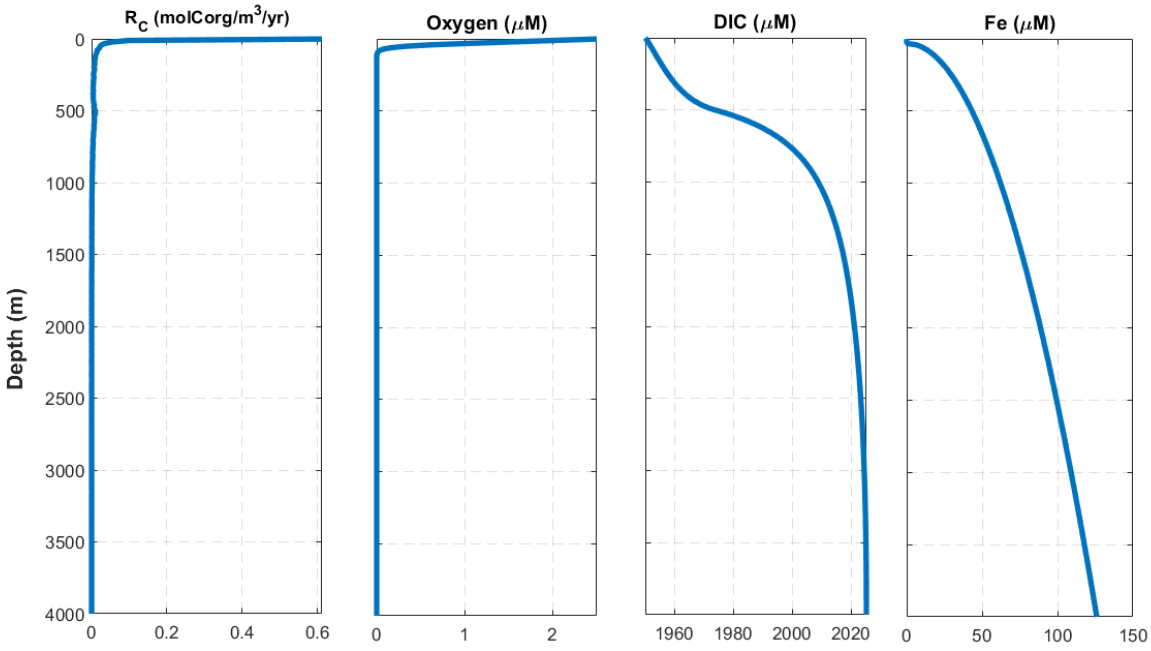

Fig. S5. Typical depth profiles of the rate of organic matter degradation using the Middleburg power law, with oxygen, DIC, and iron at estimated Proterozoic conditions – 10% of the modern productivity, 1% PAL[67], primary production dominated by picoplankton with small contribution by eukaryote algae.

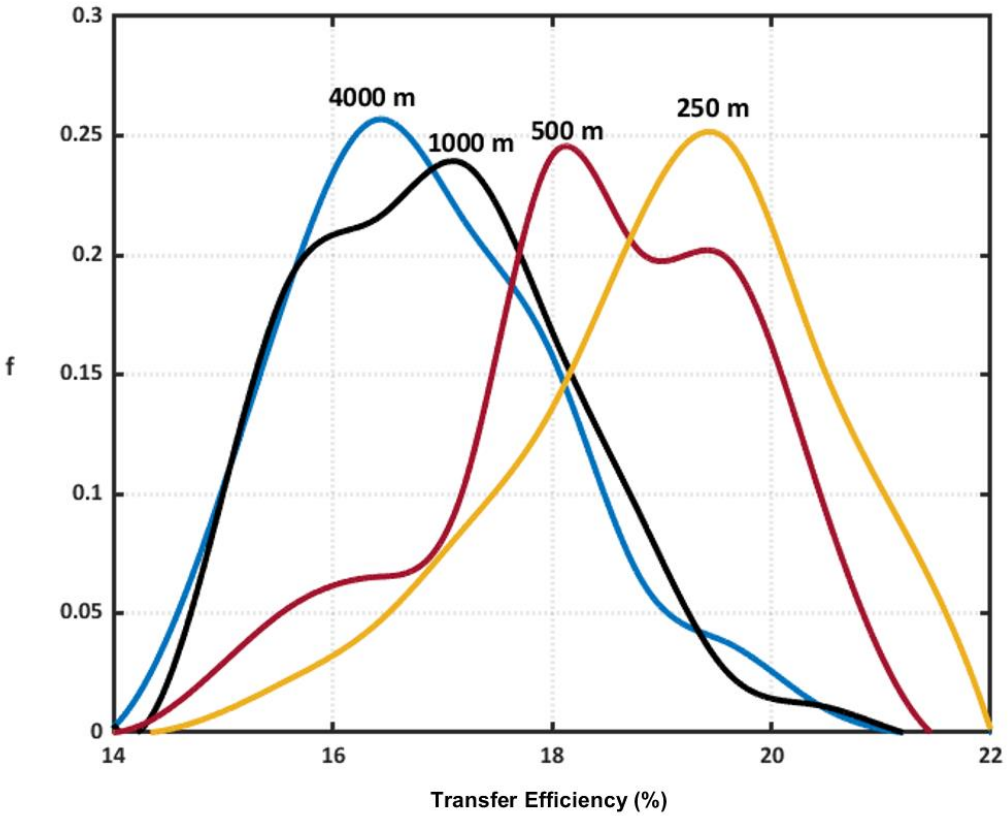

Fig S6. Probability distributions of transfer efficiency for four different depth at atmospheric oxygen level of 1% PAL and for the Precambrian-like environmental condition with high picoplankton, no algae, and high dust flux.

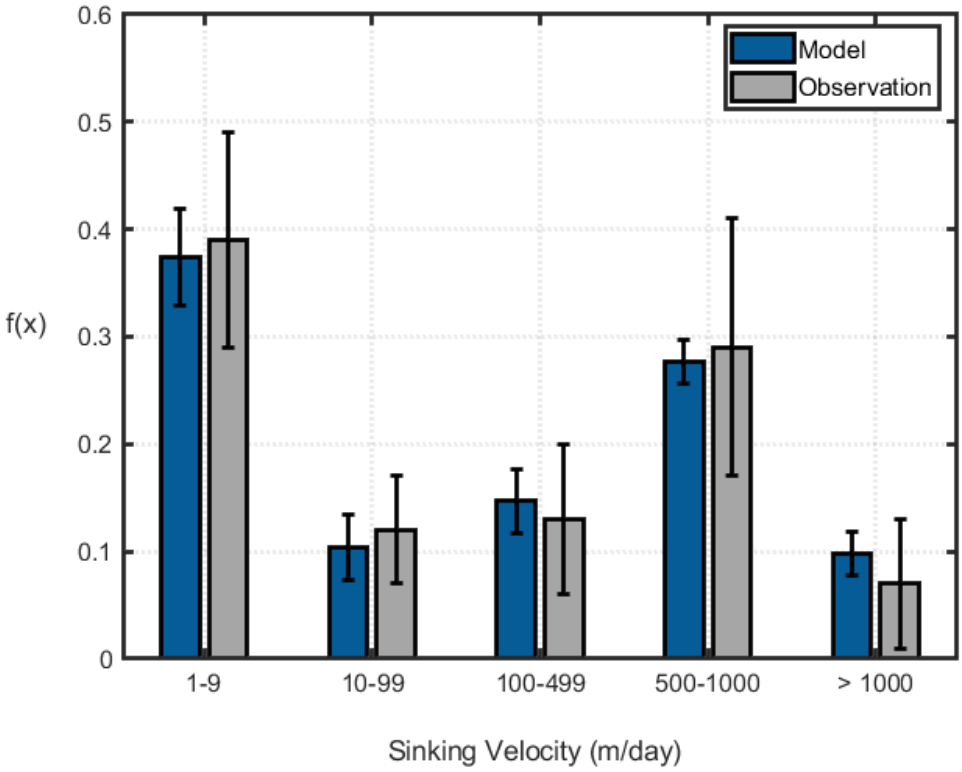

Fig. S7. Distribution of the modeled and measured settling velocity of oceanic aggregates for the modern oceans. Measured date for sinking velocity are from [22].

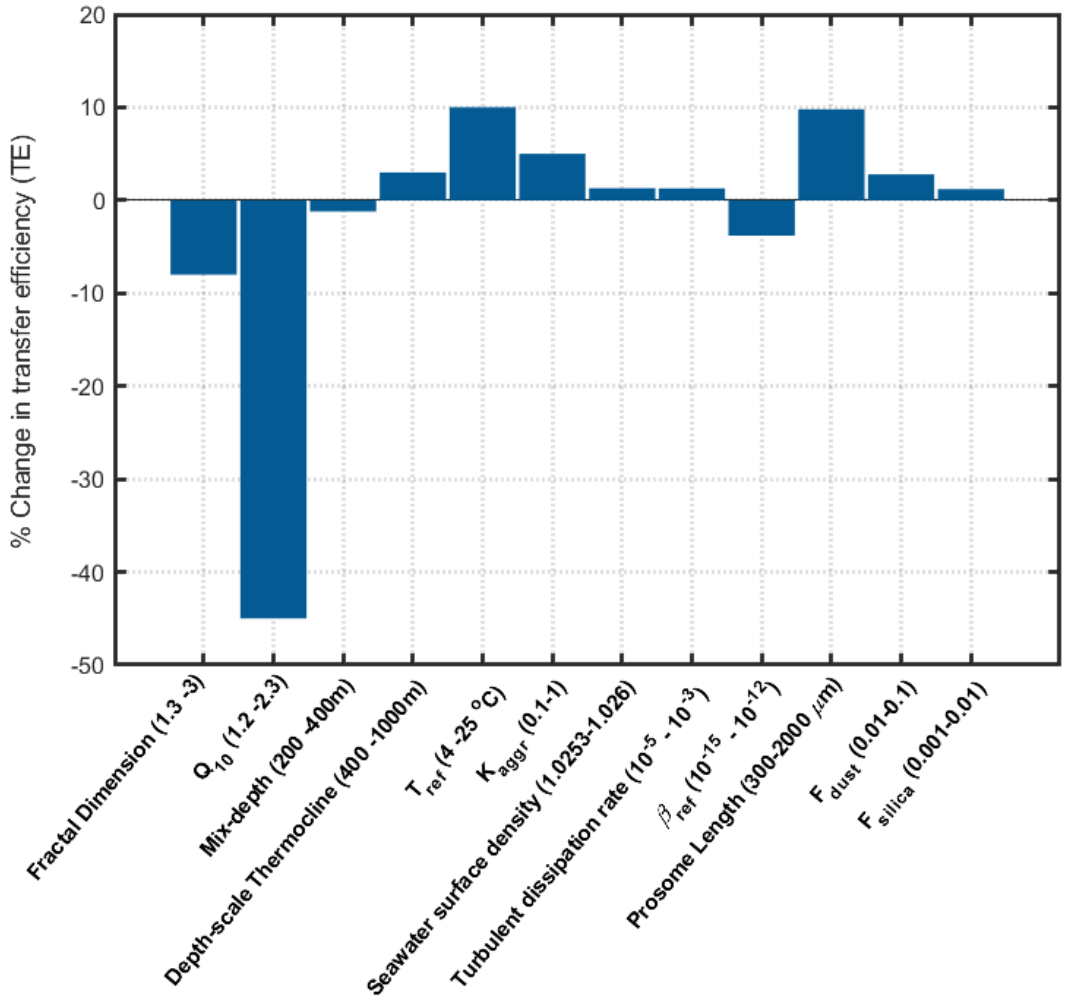

Fig S8. Change in transfer efficiency in response to variations in key model parameters under Proterozoic-like conditions: pO_2 = 10% PAL, NPP set to 20% of the modern value, high picoplankton with small contribution from algae.

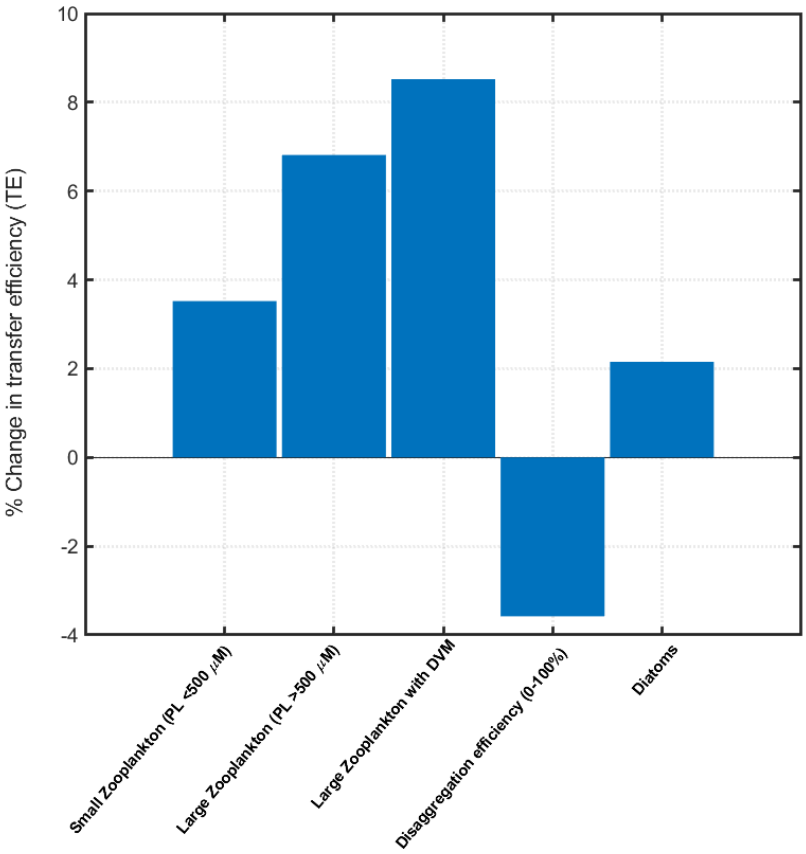

Fig S9. Change in transfer efficiency in response to variations in evolution of diatoms and different zooplankton types under Proterozoic-like conditions: pO_2 = 10% PAL, NPP set to 20% of the modern value, high picoplankton with small contribution from algae.

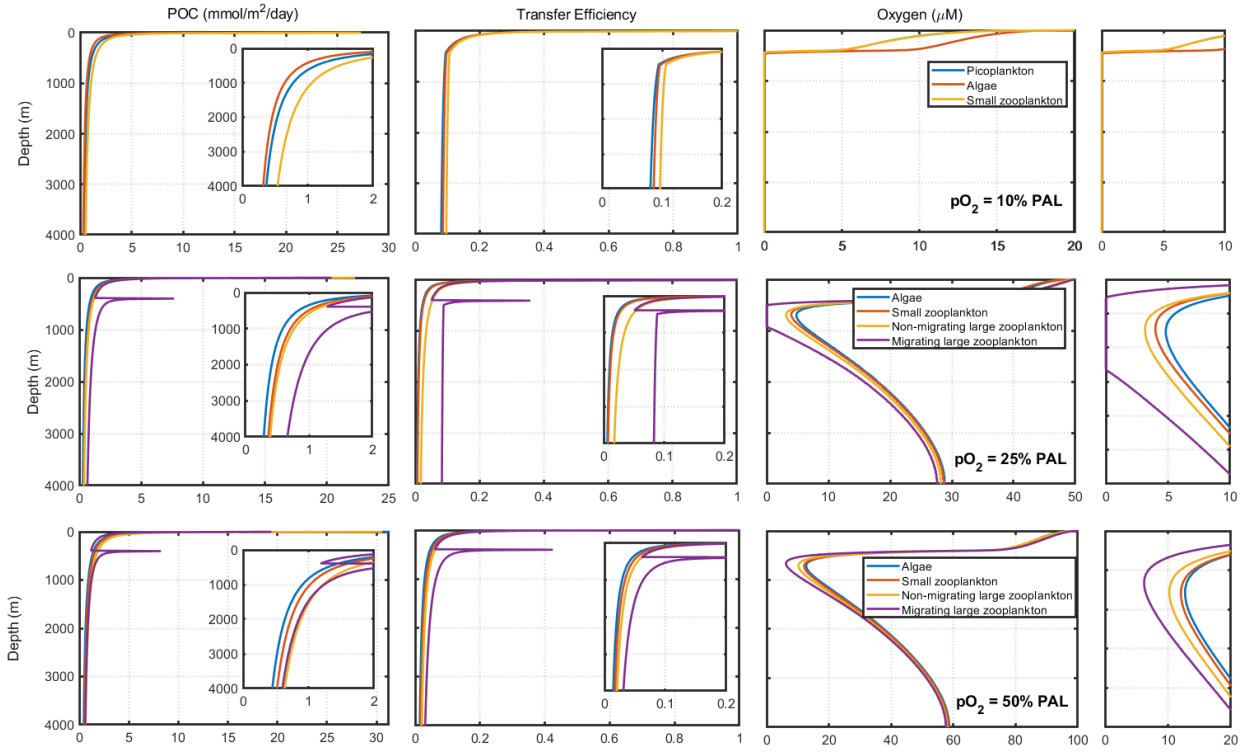

Fig. S10. Modeled depth profiles of POC, transfer efficiency, and oxygen under different biological scenarios and atmospheric oxygen levels. The evolution of larger-sized algae does not have a significant impact on the POC flux, transfer efficiency of the carbon pump, or oxygen penetration depth. The evolution of migrating large zooplankton could have enhanced the delivery of POC flux to depth, the transfer efficiency of the carbon pump, and possibility of mid-water anoxia. The largest effect on POC flux, transfer efficiency, and oxygen comes from a change in the atmospheric oxygen level.

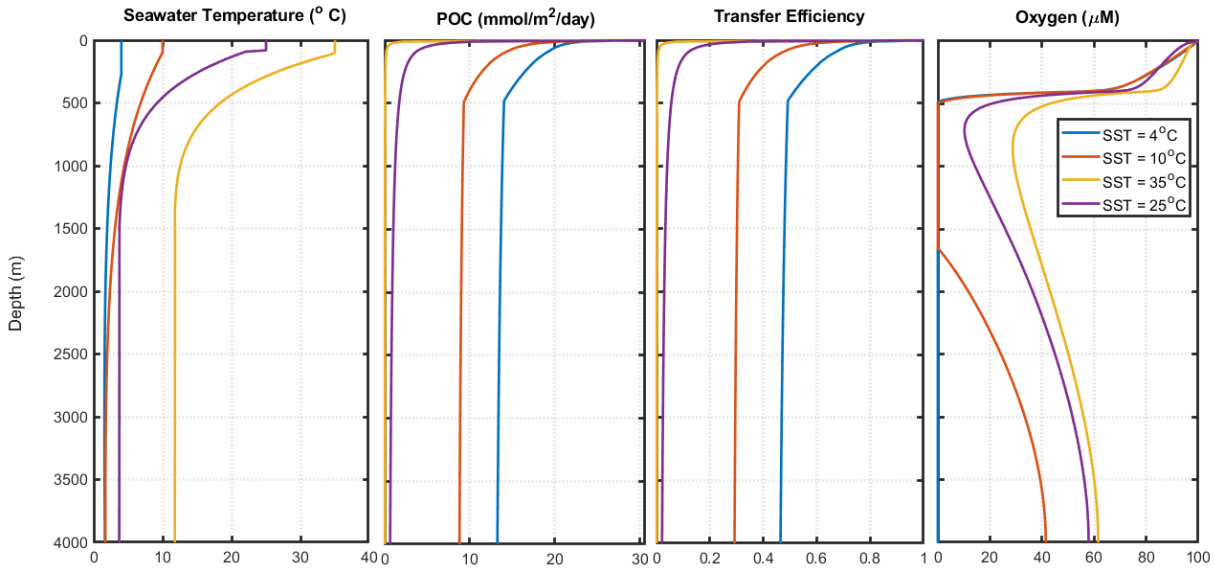

Fig. S11. Effect of seawater surface temperature on depth profiles of POC flux, transfer efficiency, and oxygen concentration. By decreasing the rate of carbon degradation, lower temperature would enhance the POC flux to depths and increase the efficiency of carbon pump. Increased POC flux at depth would result in higher rate of organic matter, increasing the possibility of anoxia in the ocean interior. Higher temperatures would result in an inefficient carbon pump with small POC flux in depths and correspondingly less anoxia. The oxygen profile at different temperatures were obtained at a fixed NPP value.

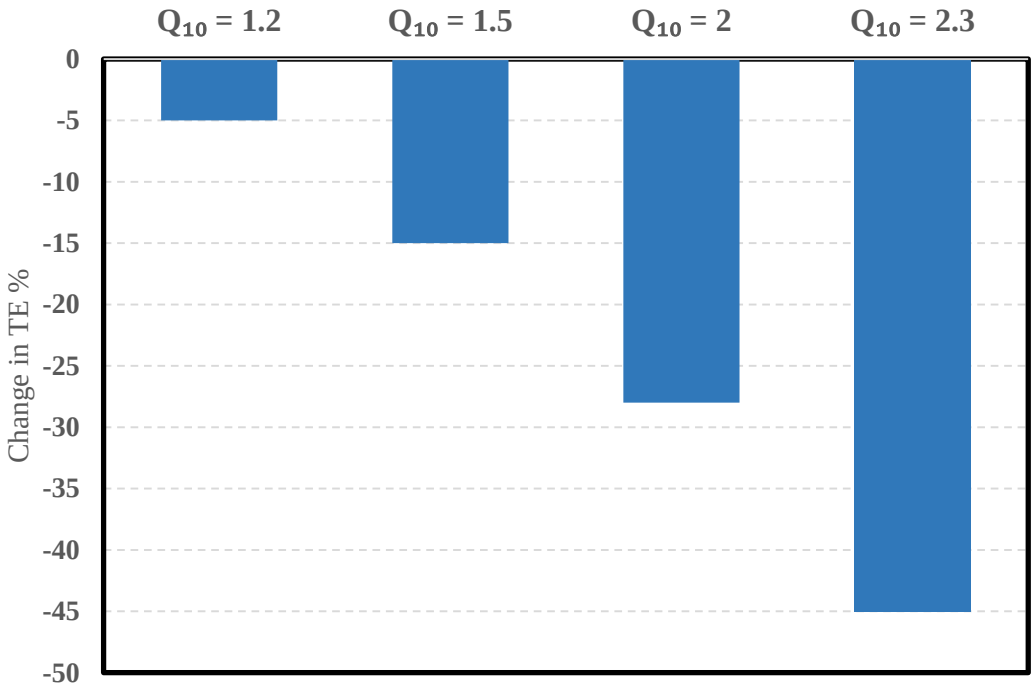

Fig S12. Change in transfer efficiency in response to 10^{o} C change in temperature for different temperature dependency factors, Q_{10} under Proterozoic-like conditions: pO_2 = 10% PAL, NPP set to 20% of the modern value, high picoplankton with small contribution from algae.

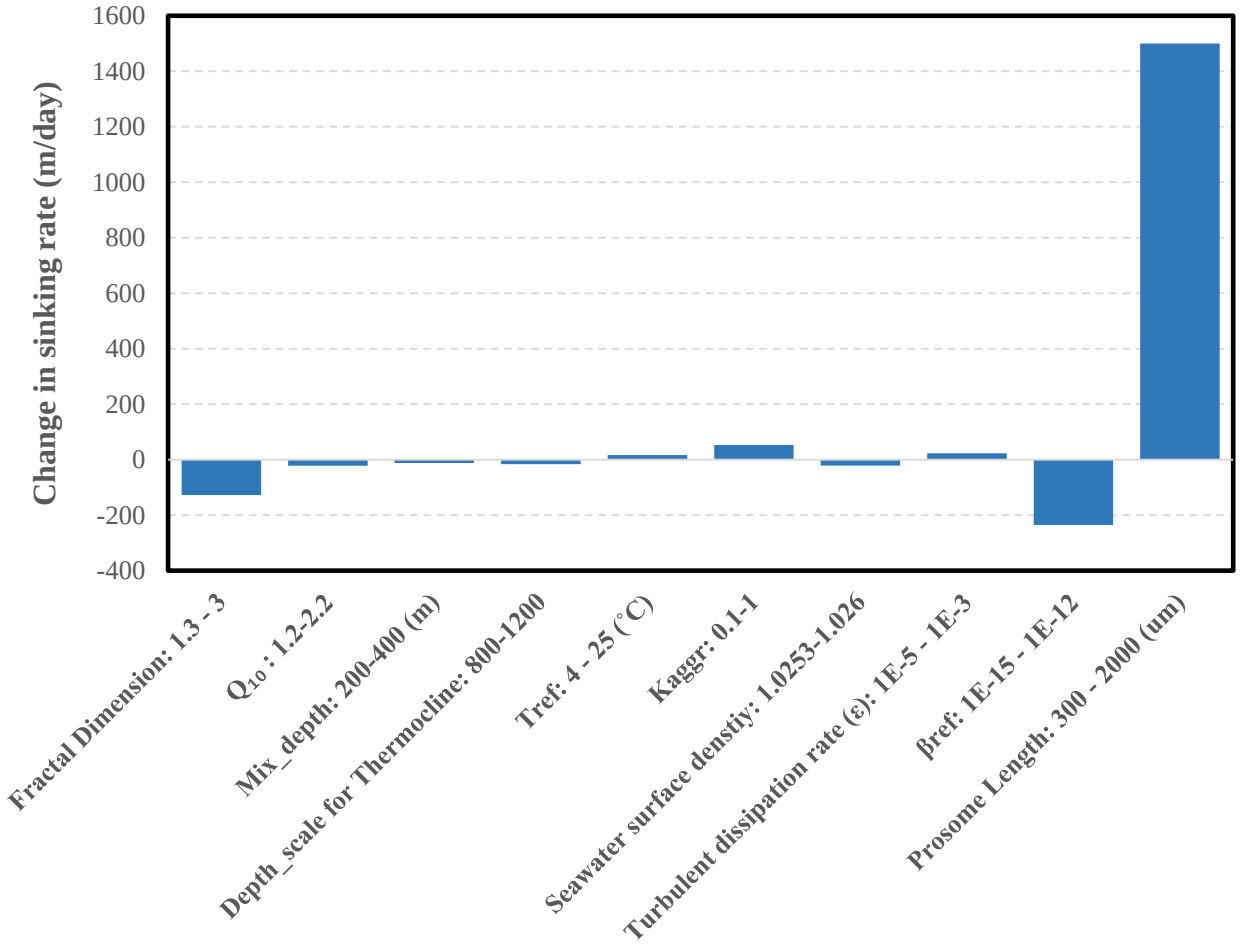

Fig S13. Change in sinking rate of aggregates at the bottom of the ocean in response to changes in model parameter values from lowest to highest values under Proterozoic-like conditions: pO_2 = 10% PAL, NPP set to 20% of the modern value, high picoplankton with small contribution from algae.